Supporting Information

Expediting hole transfer kinetics through surface state modulation of a Ru-FeOOH and $FeNi(OH)_x$ dual-layer cocatalyst coated Zr-Fe_2O_3 photoanode for boosting photoelectrochemical water splitting

Periyasamy Anushkkaran,[a] Weon-Sik Chae,[b] Jungho Ryu,*[c] Sun Hee Choi*[d] and Jum Suk Jang*[ae]

[a]Department of Integrative Environmental Biotechnology, College of Environmental and Bioresource Sciences, Jeonbuk National University, Iksan, 54596, Republic of Korea

[b]Daegu Center, Korea Basic Science Institute, Daegu 41566, Republic of Korea

[c]Mineral Resources Division, Korea Institute of Geoscience and Mineral Resources (KIGAM), Gwahak-ro 124, Yuseong-gu, Daejeon 34132, Republic of Korea

[d]Pohang Accelerator Laboratory (PAL), Pohang University of Science and Technology (POSTECH), Pohang 37673, Republic of Korea

[e]Division of Biotechnology, College of Environmental and Bioresource Sciences, Jeonbuk National University, Iksan 54896, Republic of Korea

*Corresponding authors.

E-mail address: jryu@kigam.re.kr (J. Ryu), shchoi@postech.ac.kr (S. H. Choi), jangjs75@jbnu.ac.kr (J. S. Jang)

Characterizations

X-ray diffraction (XRD) measurements were carried out for the structural analysis of the grown photoanodes at the Center for University-wide Research Facilities (CURF) at Jeonbuk National University. This analysis was performed using PANalytical X'pert Pro MPD diffractometer equipped with a Cu Kα radiation source (wavelength Kα1 = 1.540598 Å and Kα2 = 1.544426 Å) operated at 40 kV and 30 mA at a scan rate of 0.00835º 2θ s^{-1} with a 2θ angle of 20–80º. The morphology of all samples was observed using high-resolution field-emission scanning electron microscopy (HR FE-SEM, Hitachi SU8230, Korean Basic Science Institute) and high-resolution transmission electron microscopy (HR-TEM, CURF) observations were carried out. X-ray photoelectron spectroscopy (XPS) measurements were performed on a PHI Quantera II spectrometer using a monochromatic AlKα X-ray source (Kongju National University) and the binding energy was calibrated by the adventitious carbon peak of C 1s at 284.8 eV.

The TR-PL study was carried out using a confocal microscope (MicroTime-200, Picoquant, Germany) with a 40× objective. The lifetime measurements were performed at the Korea Basic Science Institute (KBSI), Daegu Center, Korea. A single-mode pulsed diode laser (470 nm with a pulse width of ~30 ps and an average power of ~75 μW) was used as an excitation source. A dichroic mirror (490 DCXR, AHF), a long-pass filter (HQ500lp, AHF), a 150 μm pinhole, and a single photon avalanche diode (PDM series, MPD) were used to collect emission from the samples. A time-correlated single-photon counting system (PicoHarp300, PicoQuant GmbH, Germany) was used to count emission photons. PL lifetime images consisted of 200×200 pixels were recorded using the time-tagged time-resolved (TTTR) data acquisition method. Exponential fitting for the obtained emission decays with a time-resolution of 8 ps was accomplished using the Symphotime-64 software (Ver. 2.2). Steady-state PL spectrum was recorded in the spectral range of 490–730 nm under 470 nm laser excitation by guiding emission photons through an optical fiber to the external spectrophotometer (F-7000, Hitachi, Japan). The time-resolved PL intensity is defined by,

$$I(t) = \sum A_i e^{-t/\tau_i} \quad \text{(S1)}$$

where, $I(t)$ is the PL intensity as a function of time, A is the amplitude, τ is the PL lifetime, and i is the subcomponent number of lifetime (1–3). The intensity-weighted average lifetime $< \tau >$ is defined as follows:[1]

$$< \tau > = \sum A_i \tau_i^2 / \sum A_i \tau_i \quad \text{(S2)}$$

Photoelectrochemical (PEC) measurements

PEC measurements were performed with an Ivium CompactStat potentiostat (Ivium Instruments, The Netherlands) in a three-electrode electrochemical cell using the prepared α-Fe_2O_3 as the working electrode, Pt wire as the counter electrode and Hg/HgO as the reference electrode. An aqueous solution of 1 M NaOH (pH = 13.6) was used as the electrolyte. Current density-potential characteristics were measured by an Ivium CompactStat potentiostat with illumination using a solar simulator with the standard global solar light (AM 1.5 G, 100 mW/cm^2). The potential was calculated against the reversible hydrogen electrode (RHE) by using the following Nernst equation:

$$E_{RHE} = E_{Hg/HgO} + 0.059pH + E^{0}_{Hg/HgO} \quad \text{(S3)}$$

($E^{0}_{Hg/HgO} = 0.095\ V$ at $25\ ^0C$)

Current density-potential curves were obtained from 0.3 to 1.7 V *vs.* RHE with a scan rate of 50 mV s^{-1}. The Nyquist plots calculated from electrochemical impedance spectroscopy (EIS) were measured at 1.23 V *vs.* RHE over the frequency range from 3000 kHz to 0.5 Hz under a 1-sun illumination condition. The incident photon-to-current efficiency (IPCE) is measured using CS130 monochromator (Mmac-200, spectro) with 300 W Xe arc lamp at 1.23 V *vs*. RHE. The IPCE of as-prepared photoanodes was calculated using the following equation:[2]

$$IPCE\ (\%) = (1240 \times J_{photo})/(I_{inc} \times \lambda) \times 100\ \% \quad \text{(S4)}$$

where, J_{photo} is the measured photocurrent density at each corresponding wavelength (mA/cm^2) at 1.23 V *vs,* RHE, I_{inc} is the incident monochromatic light power density of each corresponding wavelength (mW/cm^2) and λ is the wavelength of monochromatic light (nm) respectively. The absorbed photon-to-current efficiency (APCE) is calculated using the following equation:[3]

$$APCE = {}^{IPCE}/_{LHE} \quad \text{(S5)}$$

The water splitting (H_2 and O_2 gases evolution) was measured using a specially designed PEC three-electrode reactor. Three electrodes, namely the working electrode as a photoanode, the counter electrode as Pt wire, the and reference electrode as Hg/HgO electrodes were mounted in an airtight glass reactor that contained a quartz-glass window to allow light

illumination without any obstacle. An aqueous solution of 1 M NaOH of pH 13.6 was filled in a reactor as an electrolyte, and before the reaction started, the reactor was purged with N_2 gas (99.9%) for 1.5 h to remove dissolved oxygen. The amounts of H_2 and O_2 evolved were measured using a gas chromatography (GC) system equipped with a thermal conductivity detector (GC-TCD, Agilent 7820, USA) and a 5 Å molecular sieve column under 1-sun illumination (AM 1.5G, 100 mW/cm^2) condition at 1.23 V_{RHE}.

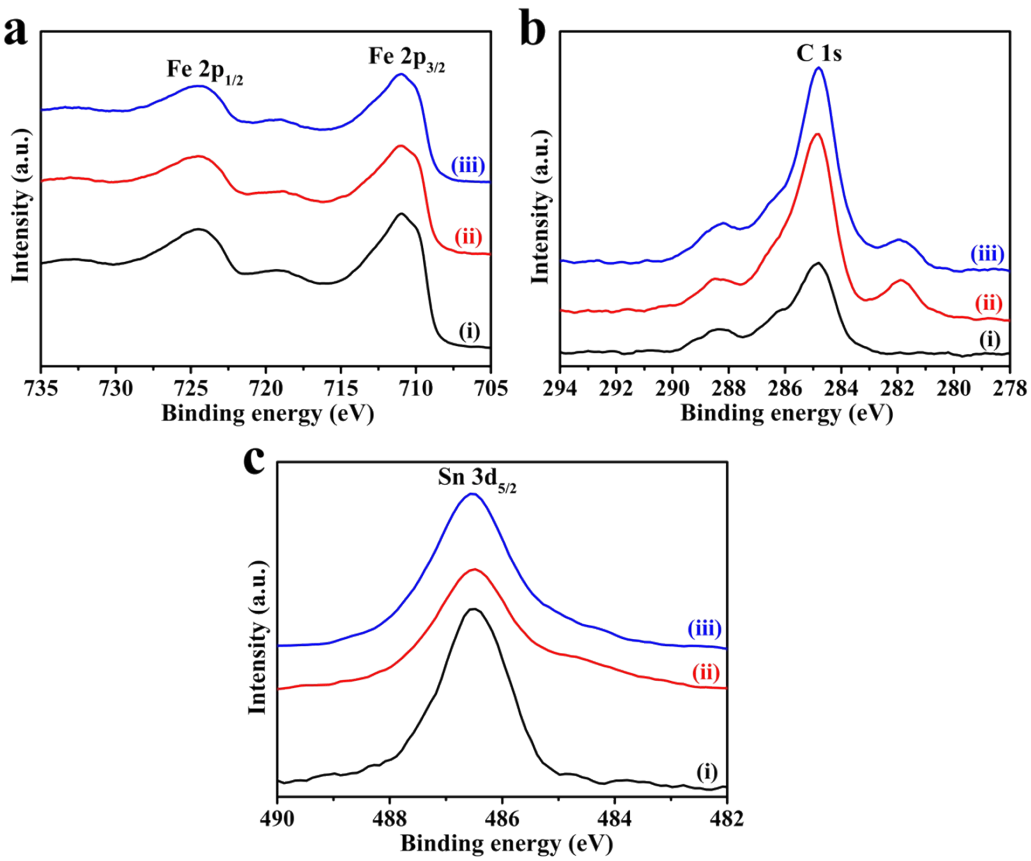

Fig. S1. XPS spectra of (a) Fe 2p, (b) C 1s and (c) Sn 3d of (i) Zr-HT, (ii) Zr-HT/Ru-FeOOH, and (iii) Zr-HT/Ru-FeOOH/FNH photoanodes.

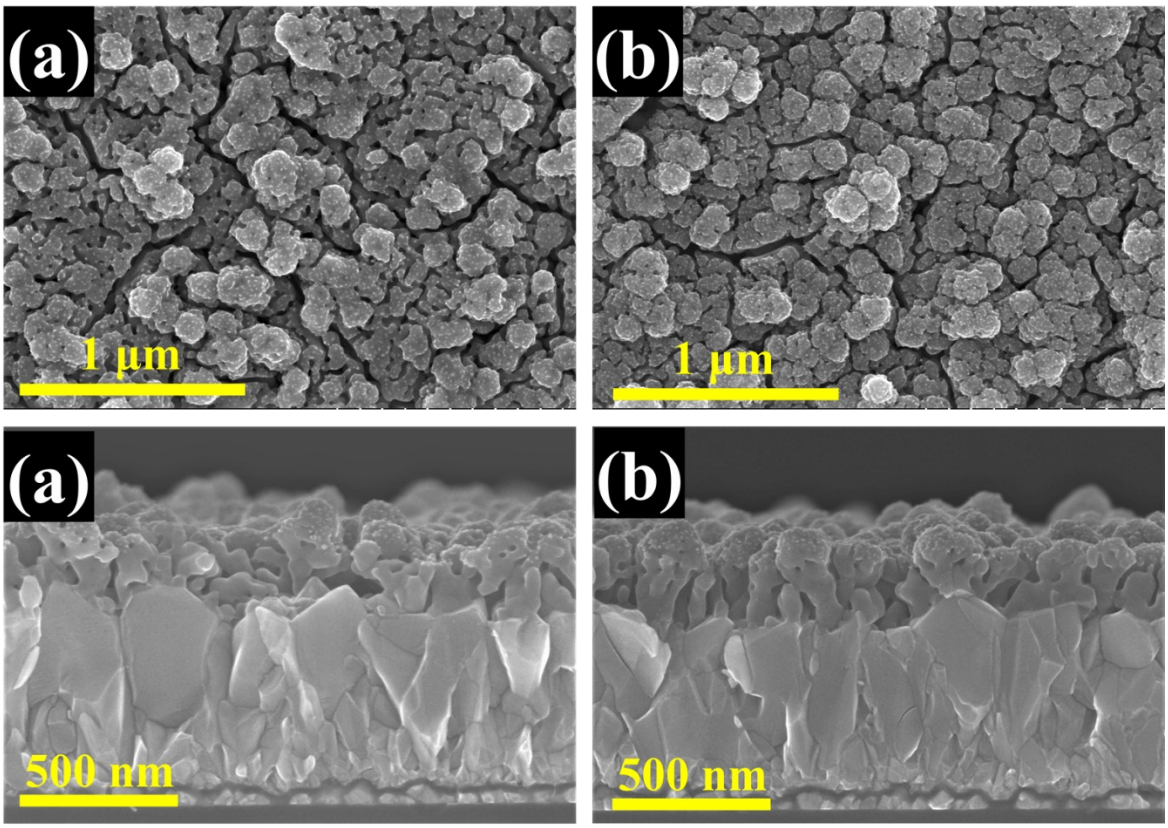

Fig. S2. HR FE-SEM top and cross-sectional images of (a) Zr-HT and (b) Zr-HT/Ru-FeOOH photoanodes.

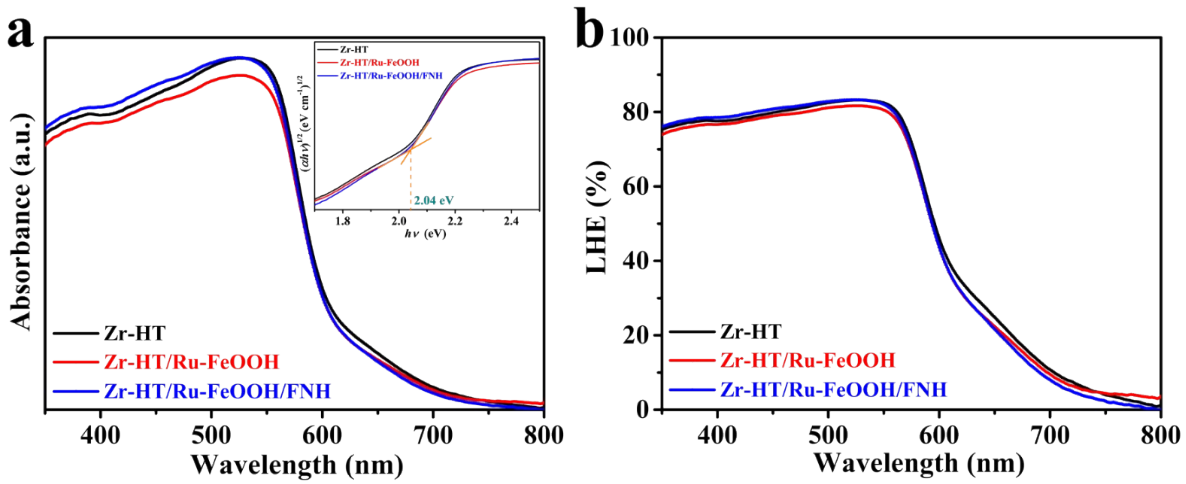

Fig. S3. (a) UV-Vis absorbance spectroscopy (inset: Tauc plots) and (b) LHE graphs of Zr-HT, Zr-HT/Ru-FeOOH, and Zr-HT/Ru-FeOOH/FNH photoanodes.

The optical properties of the as-prepared photoanodes were evaluated by ultraviolet-visible absorption spectra using a UV-Vis spectrophotometer (UV-2600, Shimadzu). The bandgap of the photoanode was determined from an indirect transition of the Tauc method:

$$(\alpha h\upsilon)^{1/n} = A(h\upsilon - E_g) \quad \text{(S6)}$$

where, α is the absorption coefficient, h is Planck's constant, υ is the photon frequency, A is a proportionality constant, E_g is the optical band gap, and n is an exponent that depends on the nature of the electronic transitions. Since hematite is an indirect bandgap semiconductor, the value of $1/n$ is 1/2.

The light harvesting efficiency (LHE; defined as the ratio of absorbed light to the incident light) of each photoanode can be calculated from the UV-Vis absorbance spectra:[4]

$$LHE = 1 - 10^{-A(\lambda)} \quad \text{(S7)}$$

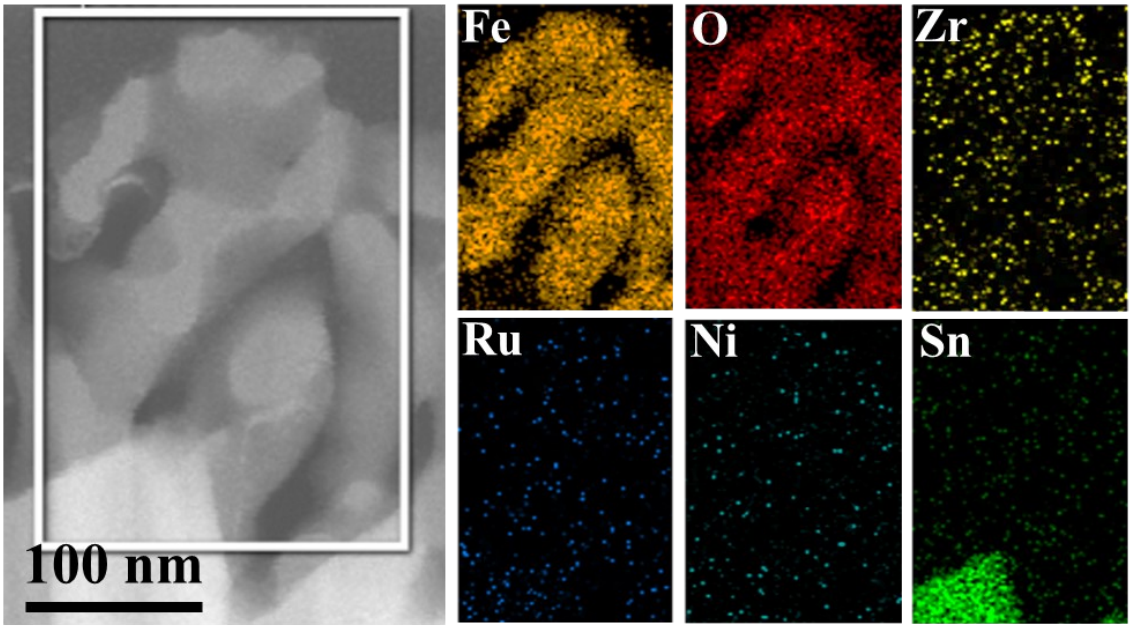

Fig. S4. EDS mapping of Zr-HT/Ru-FeOOH/FNH photoanode.

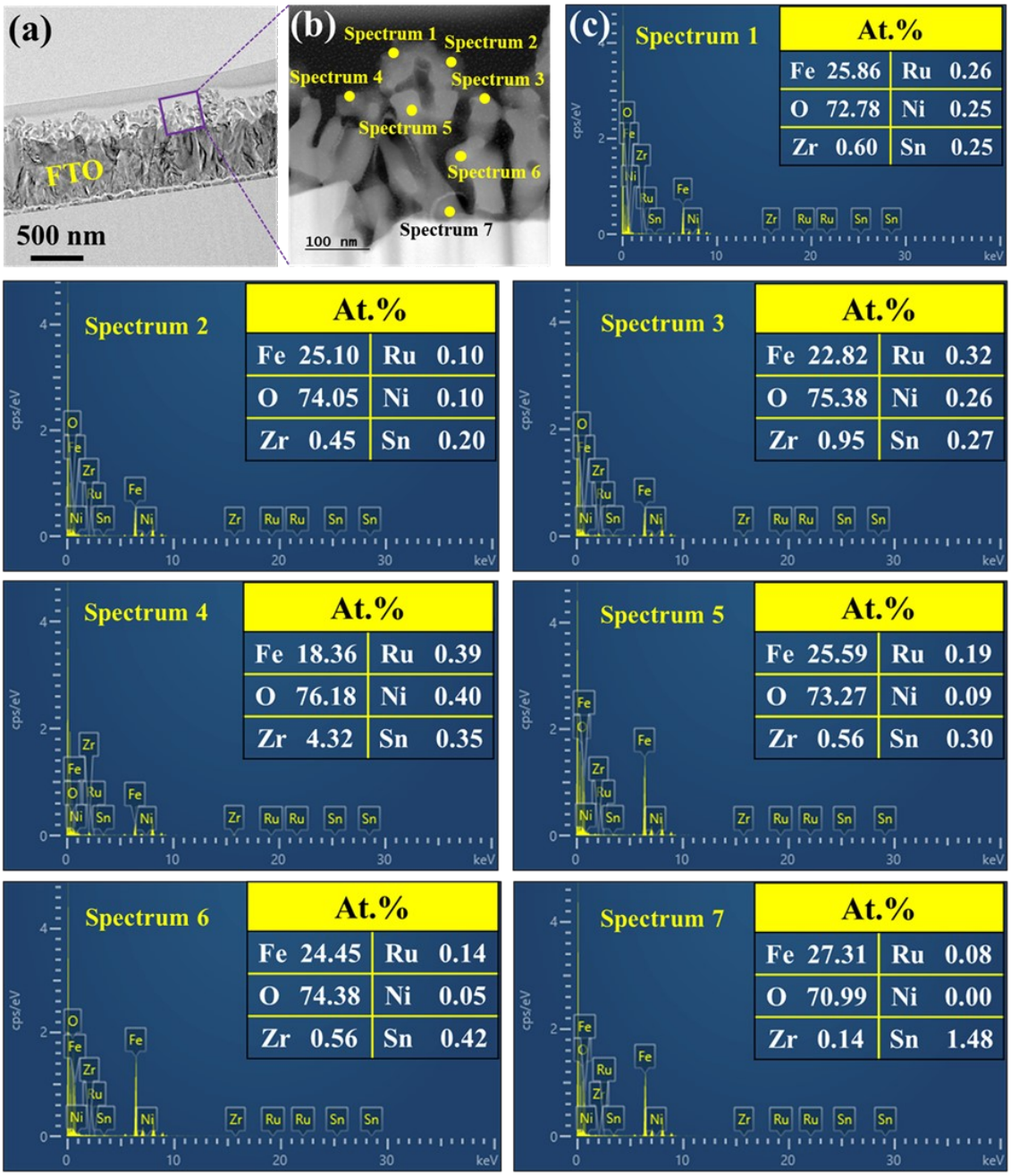

Fig. S5. (a) Low magnification TEM image, (b) Cross-sectional TEM image of Zr-HT/Ru-FeOOH/FNH photoanode and (c) respective EDS point spectra.

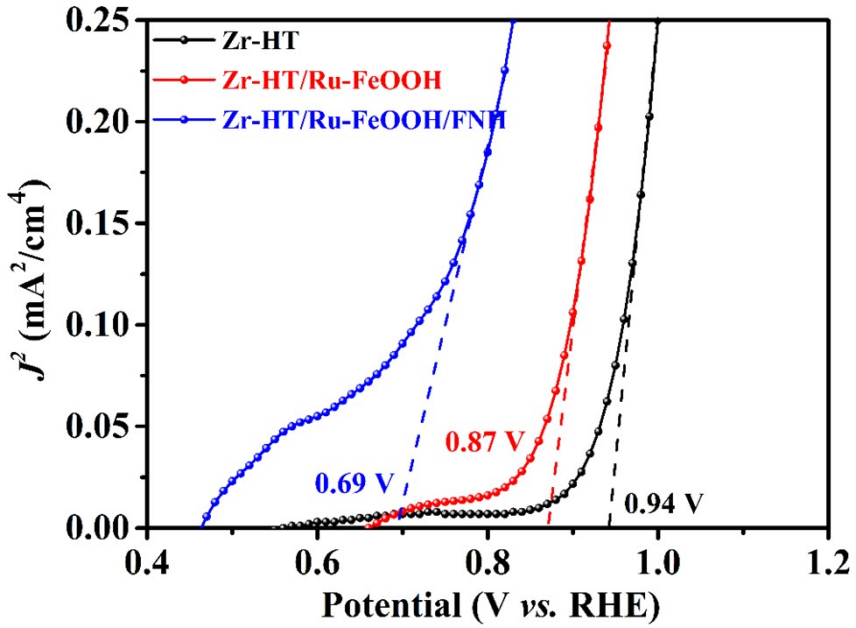

Fig. S6. Butler plots of Zr-HT, Zr-HT/Ru-FeOOH and Zr-HT/Ru-FeOOH/FNH photoanodes.

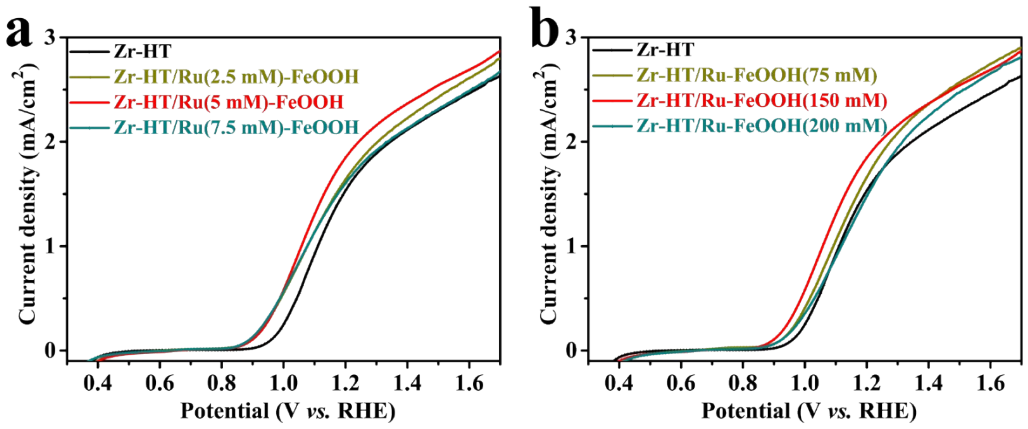

Fig. S7. *J–V* graphs of Zr-HT and Zr-HT/Ru-FeOOH with respect to (a) different Ru concentrations with 150 mM Fe and (b) various Fe concentrations with 5 mM Ru under 1-sun illumination in 1 M NaOH electrolyte.

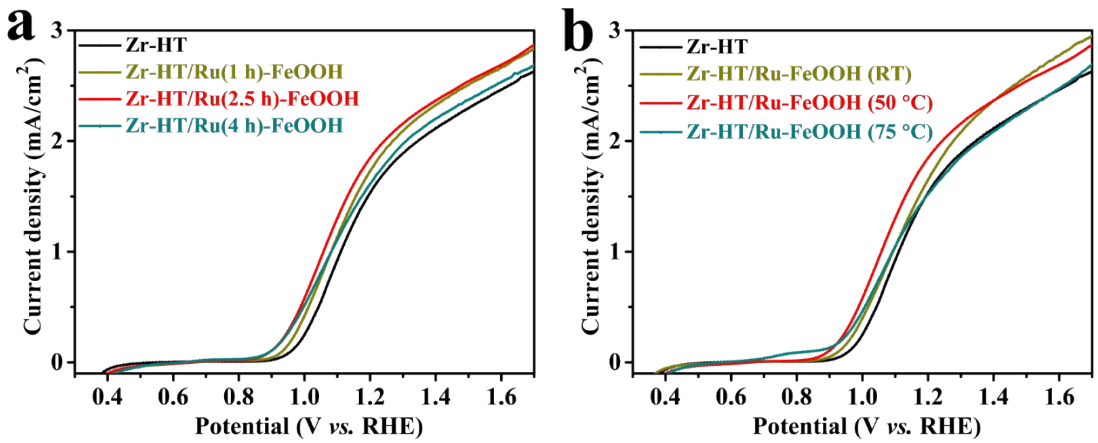

Fig. S8. *J–V* graphs of Zr-HT and Zr-HT/Ru-FeOOH with respect to different Ru-FeOOH hydrothermal (a) time at 50 ºC and (b) different hydrothermal temperatures for 2.5 h under 1-sun illumination in 1 M NaOH electrolyte.

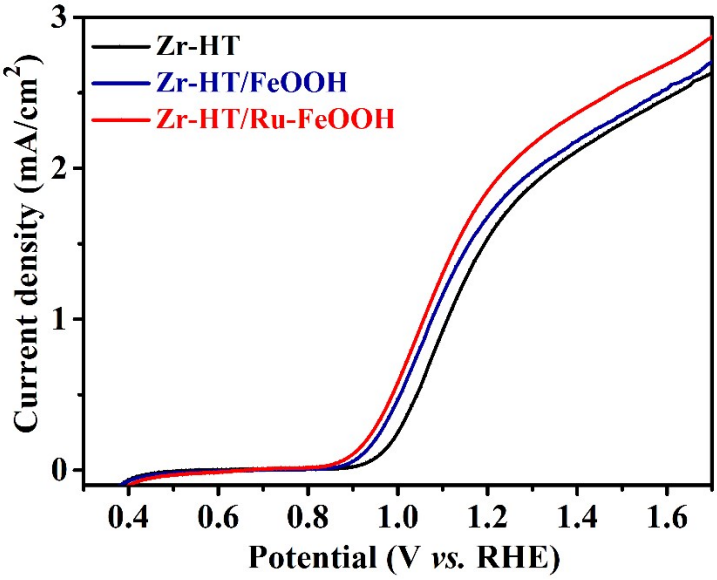

Fig. S9. *J–V* graphs of Zr-HT, Zr-HT/FeOOH and Zr-HT/Ru-FeOOH, photoanodes.

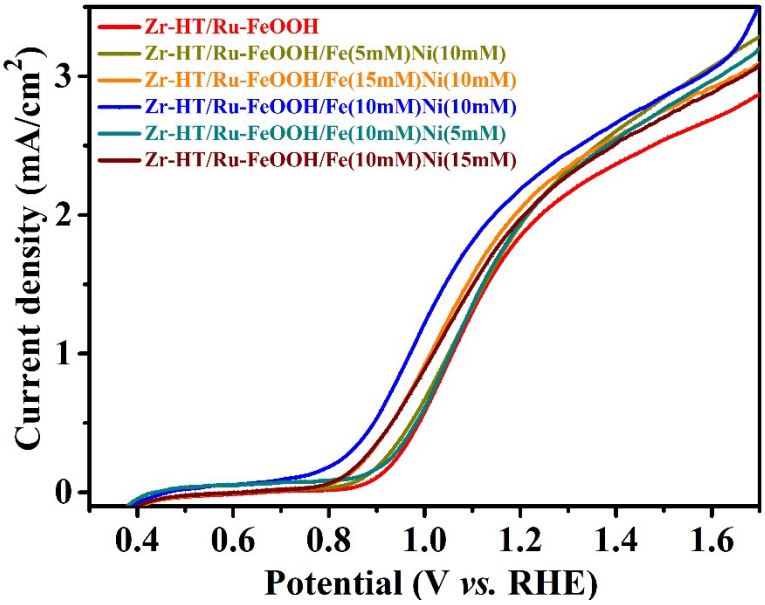

Fig. S10. *J–V* graphs of Zr-HT/Ru-FeOOH and Zr-HT/Ru-FeOOH/FNH with respect to different concentrations of $FeCl_3.6H_2O$ (5, 10 and 15 mM) and $Ni(NO_3)_2.6H_2O$ (5, 10 and 15 mM) under 1-sun illumination in 1 M NaOH electrolyte.

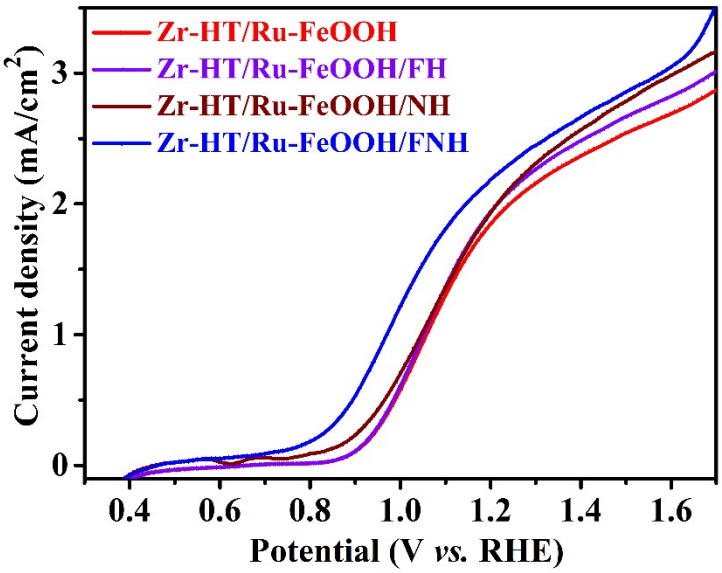

Fig. S11. *J–V* graphs of Zr-HT/Ru-FeOOH, Zr-HT/Ru-FeOOH/FH, Zr-HT/Ru-FeOOH/NH and Zr-HT/Ru-FeOOH/FNH photoanodes.

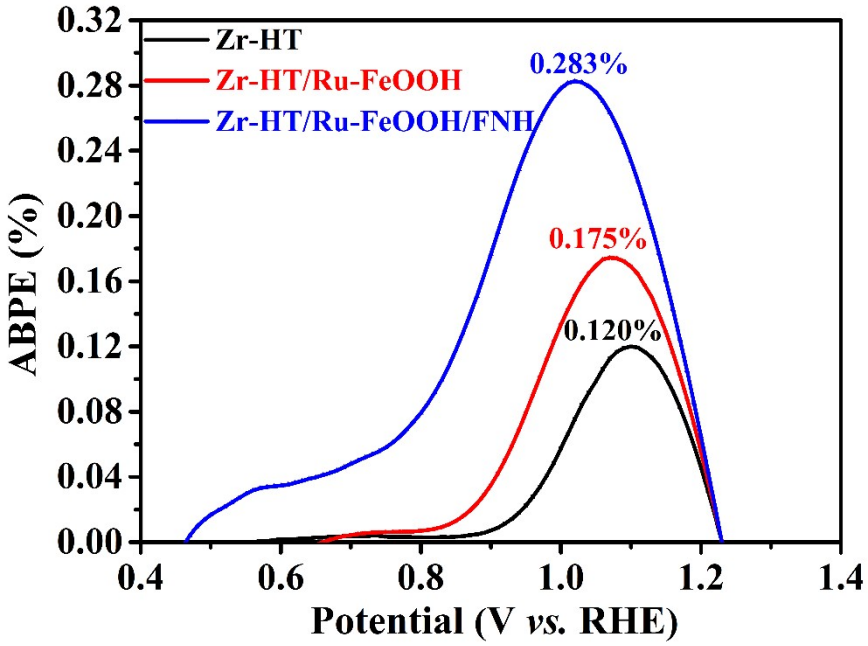

Fig. S12. ABPE plots of Zr-HT, Zr-HT/Ru-FeOOH, and Zr-HT/Ru-FeOOH/FNH photoanodes.

The applied bias photon-to-current efficiency (ABPE) was calculated using the following equation:

$$\text{ABPE}\ (\%) = J_{ph} \times [(1.23 - V)/P] \times 100 \qquad \text{(S8)}$$

where, J_{ph} is the photocurrent density (mA/cm^2), V is the applied potential of the working electrode under illumination *vs.* RHE and P is the incident light intensity of the solar simulator (100 mW/cm^2).

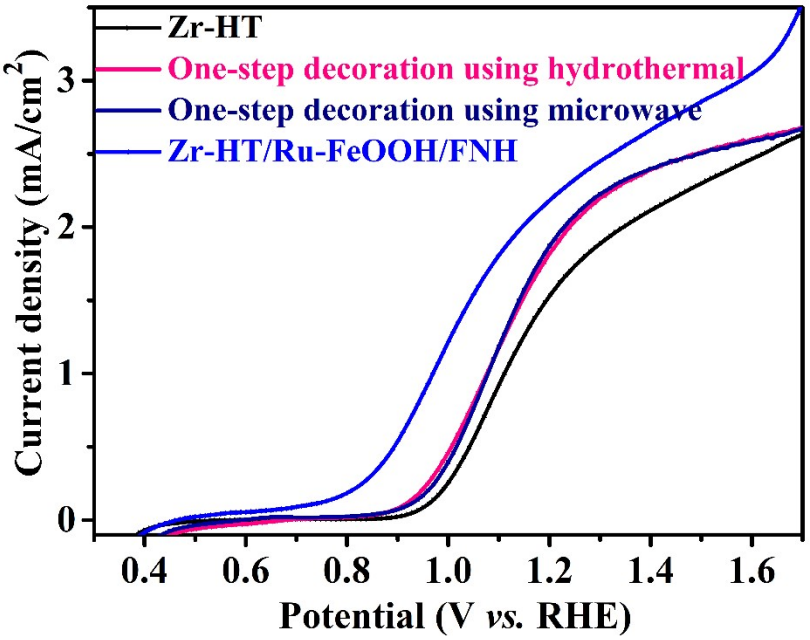

Fig. S13. Photocurrent density-potential (*J–V*) curves under 1-sun illumination of Zr-HT, a complex of Ru-FeOOH and $FeNi(OH)_x$ one-step deposition using hydrothermal and microwave, and Zr-HT/Ru-FeOOH/FNH photoanodes.

As shown in Fig. S13, Ru-FeOOH and $FeNi(OH)_x$ one-step deposition on Zr-HT photoanode via hydrothermal and microwave approaches reached the photocurrent density of 1.96 mA/cm^2 and 2.0 mA/cm^2, respectively, at 1.23 V_{RHE}. These photocurrents are significantly lower than that of dual-layer cocatalyst samples (Zr-HT/Ru-FeOOH/FNH). Besides, these photoanodes exhibited a marginal cathodic onset shifting as compared to Zr-HT. From this observation, we can conclude that the two-step cocatalyst modification is preferable for effective PEC water oxidation than the one-step cocatalyst decoration.

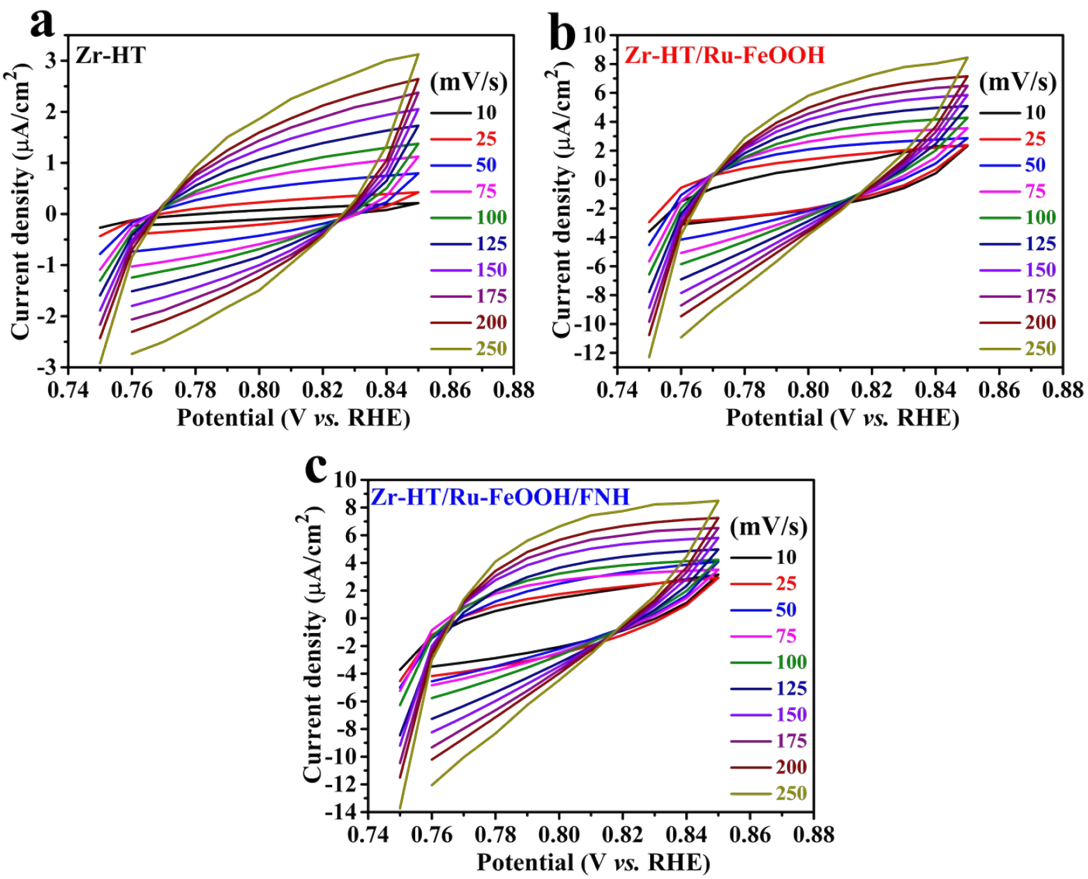

Fig. S14. CV were obtained in the non-faradaic potential region of 0.75–0.85 V_{RHE} at various scan rates ranging from 10 to 250 mV/s for (a) Zr-HT, (b) Zr-HT/Ru-FeOOH and (c) Zr-HT/Ru-FeOOH/FNH photoanodes using 1 M NaOH electrolyte.

The electrochemically active surface area (ECSA) was determined using double-layer capacitance (C_{dl}) measurements at 10 different scan rates (10, 25, 50, 75, 100, 125, 150, 175, 200 and 250 mV/s) in the non-faradaic region of 0.75–0.85 V_{RHE} by using cyclic voltammograms (Fig. S14). The C_{dl} values were evaluated by plotting the corresponding absolute current *vs.* scan rate plot obtained at 0.80 V_{RHE}. The slopes of the fitting line can be used to estimate the C_{dl} of the as-prepared photoanodes, as the slope is twice the C_{dl}. The ECSA was then computed using the following formula based on the obtained C_{dl} values:[6]

$$ECSA = {}^{C_{dl}}/_{C_s} \qquad \text{(S9)}$$

where, C_s is the specific capacitance of the sample, which is 40 μF/cm^2 in 1 M NaOH electrolyte.

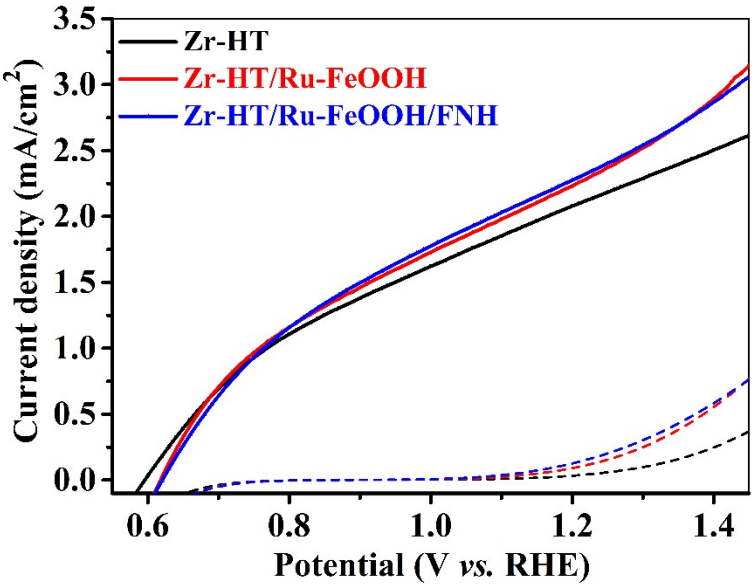

Fig. S15. *J–V* plots of Zr-HT, Zr-HT/Ru-FeOOH, and Zr-HT/Ru-FeOOH/FNH photoanodes in 0.5 M H_2O_2 + 1 M NaOH electrolyte under 1-sun illumination and dark condition (dashed lines).

The bulk charge separation efficiency (η_{bulk}) and surface charge separation efficiency ($\eta_{surface}$) of as-synthesized photoanodes were measured by the addition of 0.5 M H_2O_2 in 1 M NaOH electrolyte solution. The η_{bulk} and $\eta_{surface}$ were calculated by the following equations:[7]

$$\eta_{bulk} = J_{H_2O_2}/J_{abs} \times 100 \quad \text{(S10)}$$

$$\eta_{surface} = J_{H_2O}/J_{H_2O_2} \times 100 \quad \text{(S11)}$$

where, J_{H2O} is the measured photocurrent density, J_{abs} is the photon absorption expressed as a current density (i.e., absorbed photon-to-current efficiency APCE =100%), and J_{H2O2} is the photocurrent density in the presence of H_2O_2.

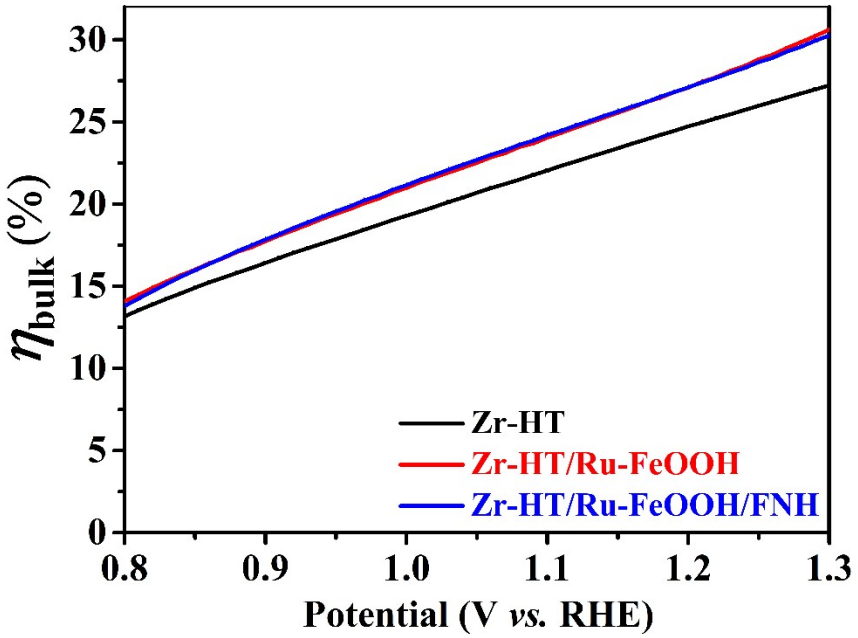

Fig. S16. Bulk charge separation efficiencies of Zr-HT, Zr-HT/Ru-FeOOH, and Zr-HT/Ru-FeOOH/FNH photoanodes.

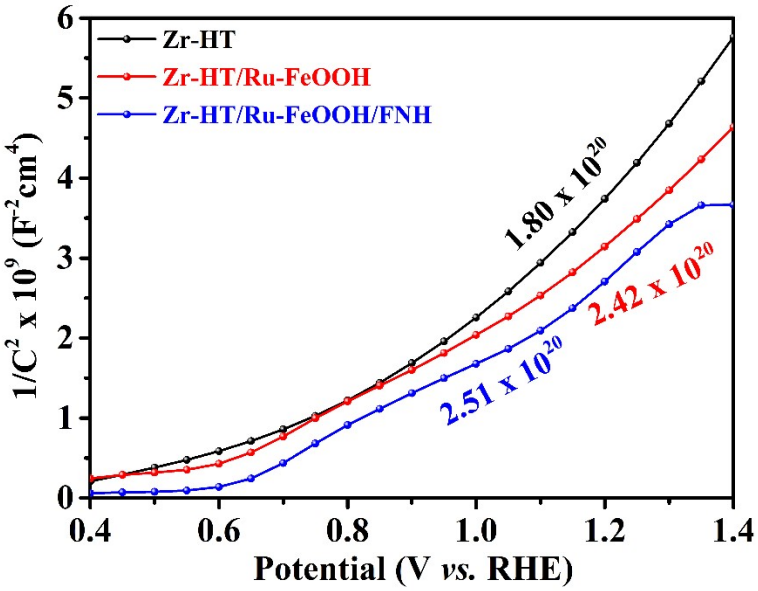

Fig. S17. Mott-Schottky plots under dark conditions for Zr-HT, Zr-HT/Ru-FeOOH, and Zr-HT/Ru-FeOOH/FNH photoanodes.

The Mott-Schottky plots were measured in dark conditions at a frequency of 100 Hz to understand the donor density (N_D) and flat band potential based on the following equation:[8]

$$1/C^2 = \frac{2}{q\varepsilon\varepsilon_0 N_D A^2}(V - E_{FB} - k_B T/q) \quad \text{(S12)}$$

where, q is the electron charge (1.602×10^{-19} C), ε is the dielectric constant of hematite (80), ε_0 is the permittivity of vacuum (8.854×10^{-12} F m^{-1}), E_{FB} is the flat band potential, k_B is the Boltzmann constant (1.38×10^{-23} J K^{-1}), T is the temperature and C is the capacitance derived from the electrochemical impedance obtained at each potential (V).

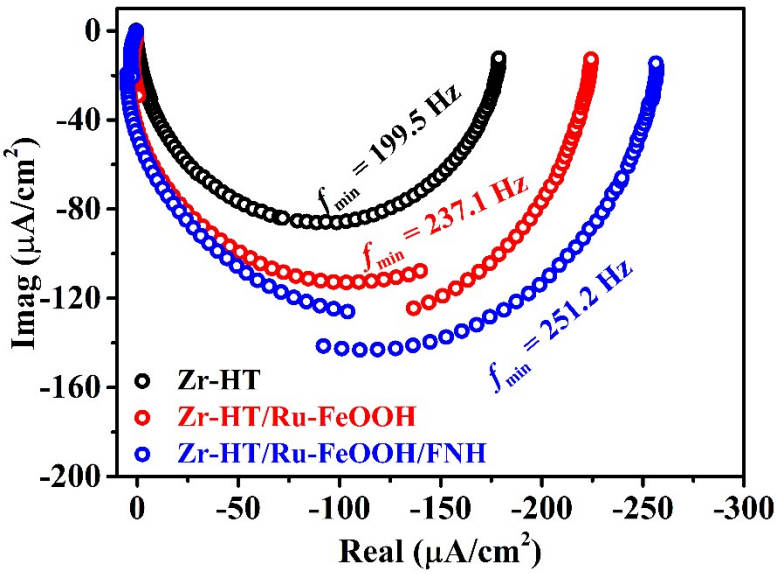

Fig. S18. IMPS plots at 1.23 V_{RHE} for Zr-HT, Zr-HT/Ru-FeOOH, and Zr-HT/Ru-FeOOH/FNH photoanodes.

The intensity-modulated photocurrent spectroscopy (IMPS) study was performed using a blue LED by a frequency-response analyzer with a peak wavelength of 460 nm. The average transport time of the photogenerated electron (τ_{et}) can be calculated from the angular frequency of the minimum given by the following equation:[9]

$$\tau_{et} = (2\pi f_{min})^{-1} \quad \text{(S13)}$$

where, f_{min} is the frequency at the minimum imaginary component in the IMPS semicircle.

Table S1. Frequency at the minimum imaginary component (f_{min}) and average electron transport time (τ_{et}) in the IMPS spectra for Zr-HT, Zr-HT/Ru-FeOOH, and Zr-HT/Ru-FeOOH/FNH photoanodes at 1.23 V *vs.* RHE.

Samples	f_{min} (Hz)	τ_{et} (ms)
Zr-HT	199.5	0.79
Zr-HT/Ru-FeOOH	237.1	0.67
Zr-HT/Ru-FeOOH/FNH	251.2	0.63

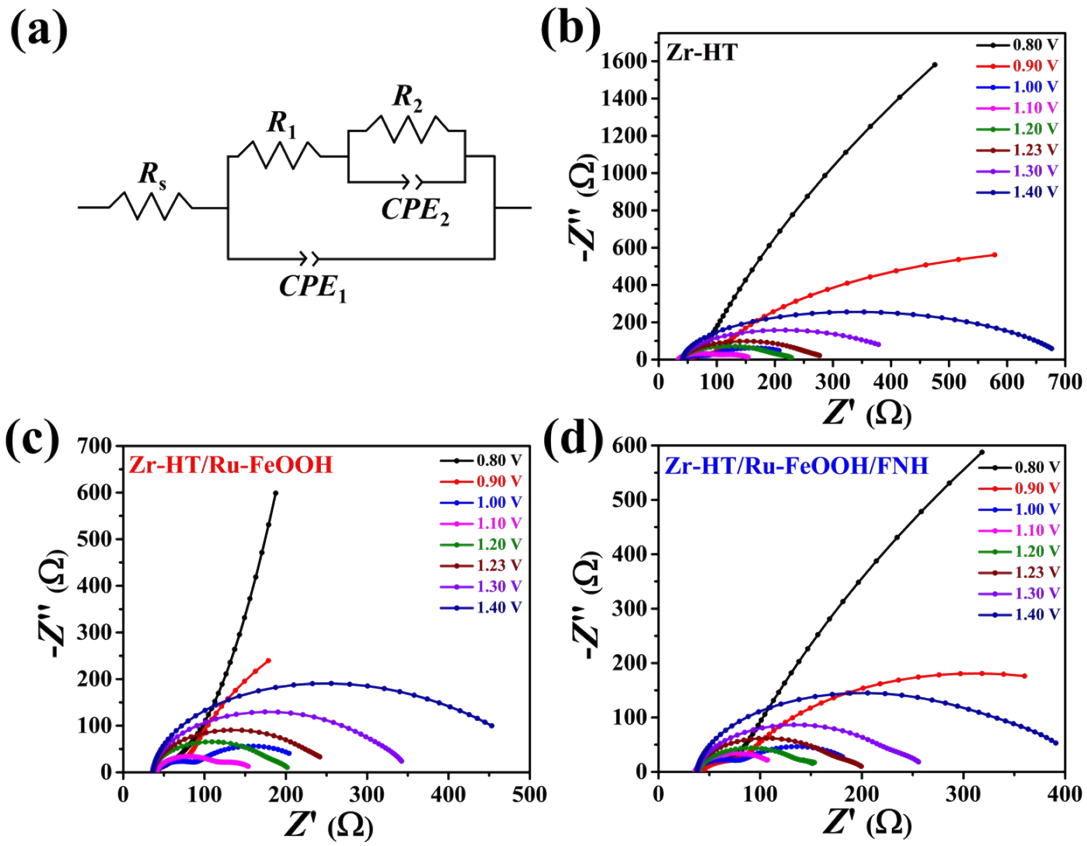

Fig. S19. (a) Nyquist plots fitted circuit model, EIS curves of (b) Zr-HT, (c) Zr-HT/Ru-FeOOH, and (d) Zr-HT/Ru-FeOOH/FNH photoanodes at various potentials.

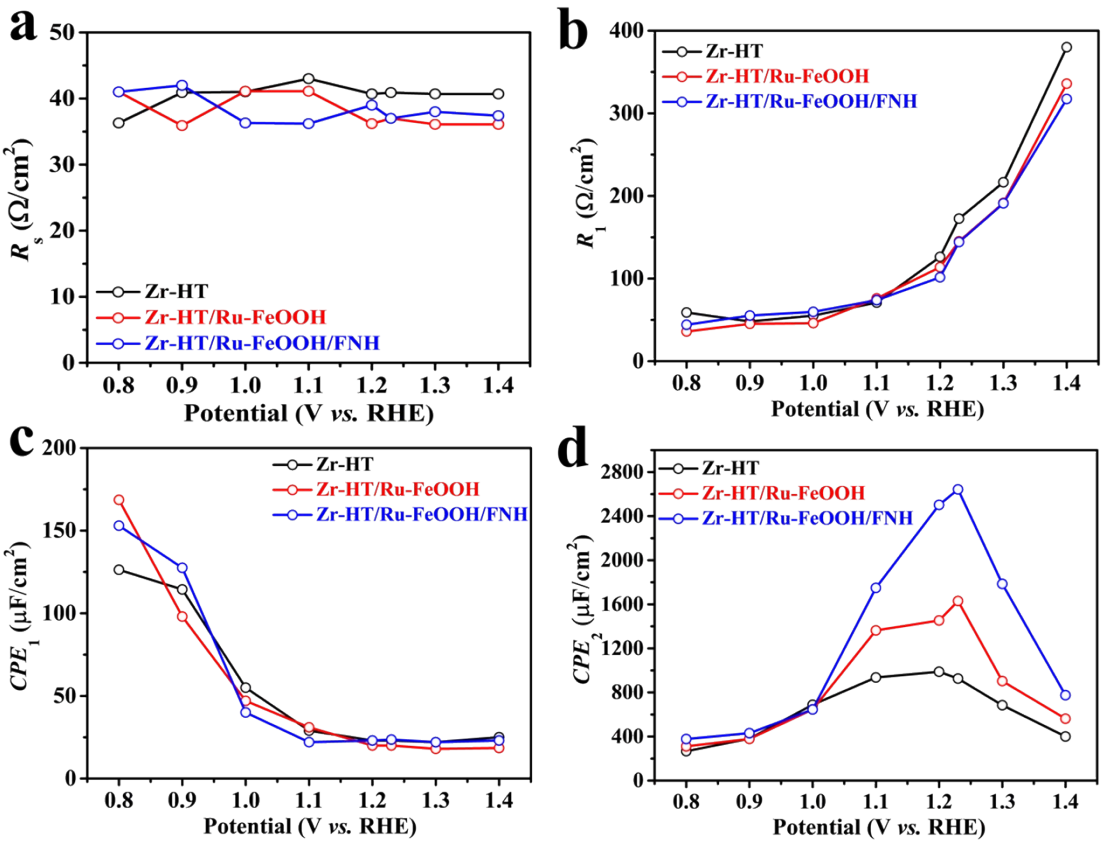

Fig. S20. (a) R_s, (b) R_1, (c) CPE_1 and (c) CPE_2 values of Zr-HT, Zr-HT/Ru-FeOOH, and Zr-HT/Ru-FeOOH/FNH photoanodes at various potentials.

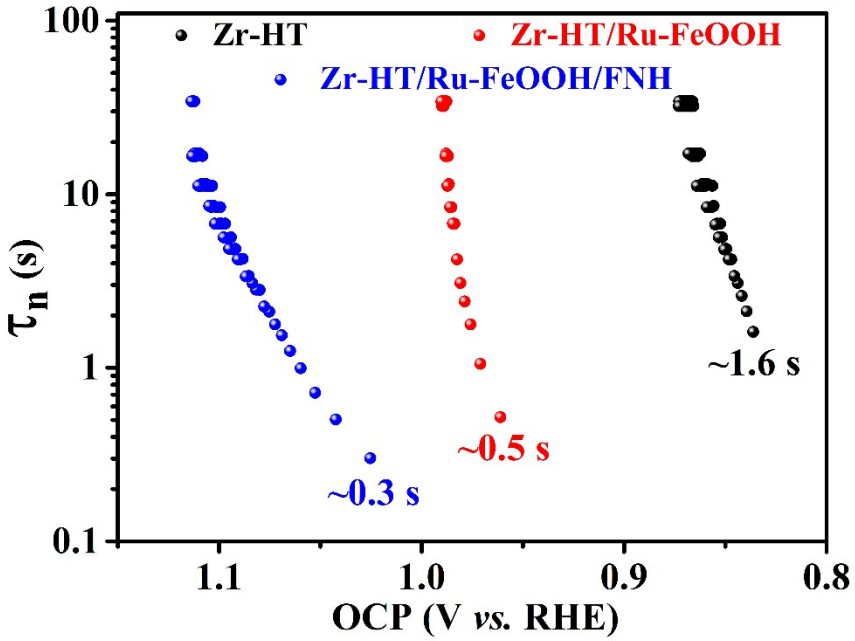

Fig. S21. Potential dependent carrier lifetime for Zr-HT, Zr-HT/Ru-FeOOH and Zr-HT/Ru-FeOOH/FNH photoanodes at various potentials.

The carrier lifetime of the photogenerated charges (τ_n) as a function of OCP was evaluated using the following equation:[10]

$$\tau_n = \frac{k_B T}{e}\left(\frac{dOCP}{dt}\right)^{-1} \quad \text{(S14)}$$

where, k_B, T, e and dOCP/dt are Boltzmann's constant, Kelvin temperature, a charge of the electron and derivative of the OCP transient decay, respectively.

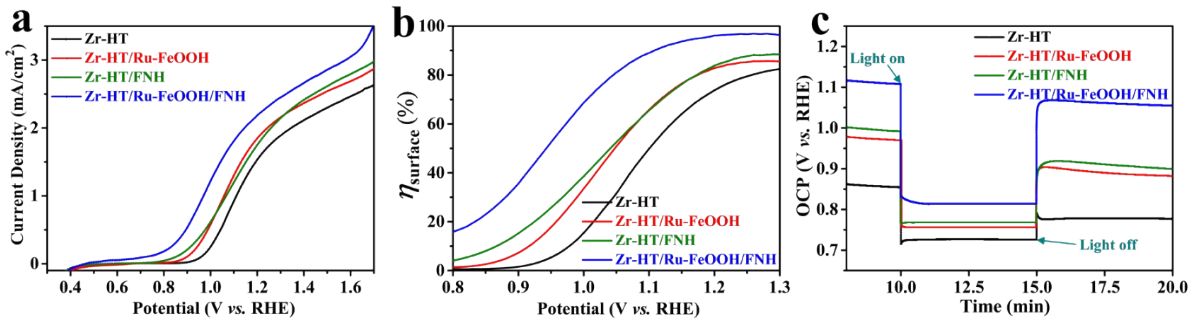

Fig. S22. (a) *J–V* graphs, (b) $\eta_{surface}$ and (c) OCP plots of Zr-HT, Zr-HT/Ru-FeOOH, Zr-HT/FNH and Zr-HT/Ru-FeOOH/FNH photoanodes.

Ru-FeOOH and $FeNi(OH)_x$ dual-cocatalyst layer deposited on Zr-Fe_2O_3 photoanode exhibited enhanced PEC activity than only $FeNi(OH)_x$ coated Zr-Fe_2O_3 photoanode. This can be attributed to the intermediate Ru-FeOOH layer facilitating the surface charge separation and thereby hastening the hole transfer to the surface of the photoanode via $FeNi(OH)_x$ layer. This observation was further evidenced by the surface charge separation efficiency (Fig. S22b). Moreover, the cathodic OCP_{dark} value of the Zr-HT/FNH photoanode compared to that of Zr-HT/Ru-FeOOH/FNH further corroborated the existence of Fermi level pinning effect in Zr-HT/FNH photoanode (Fig. S22c), which restricted the effective charge separation and charge transfer.

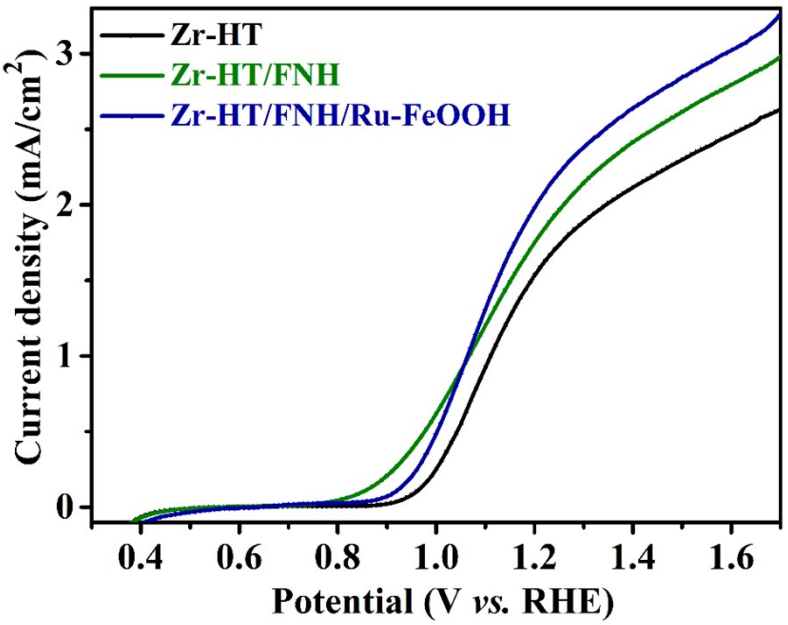

Fig. S23. *J–V* graphs of Zr-HT, Zr-HT/FNH and Zr-HT/FNH/Ru-FeOOH photoanodes.

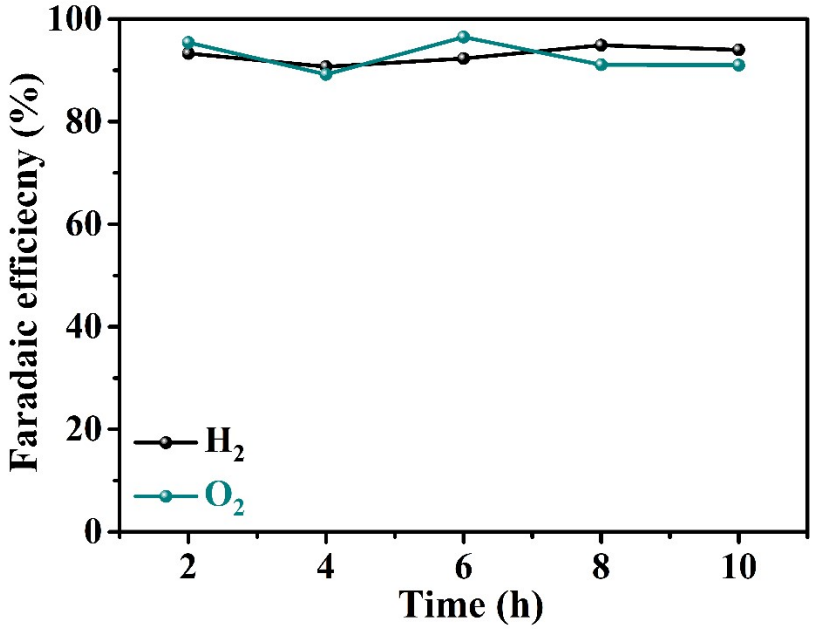

Fig. S24. Faradaic efficiencies of Zr-HT/Ru-FeOOH/FNH photoanode.

The corresponding OER steps in alkaline solution are described as below:

$$* + OH^- + h^+ \rightarrow OH^* + e^- \quad \text{(S15)}$$

$$OH^* + OH^- + h^+ \rightarrow O^* + H_2O + e^- \quad \text{(S16)}$$

$$O^* + OH^- + h^+ \rightarrow OOH^* + e^- \quad \text{(S17)}$$

$$OOH^* + OH^- + h^+ \rightarrow O_2 + H_2O + * + e^- \quad \text{(S18)}$$

where, * represents the surface-active sites (metal active sites), and OH*, O* and OOH* are the reaction intermediates.

References

1. J. B. Hwang, M. A. Mahadik, P. Anushkkaran, S. H. Choi, W. S. Chae, H. H. Lee and J. S. Jang, *Appl. Surf. Sci.*, 2022, **596,** 153609.
2. M. A. Gaikwad, U. V. Ghorpade, U. P. Suryawanshi, P. V. Kumar, S. Jang, J. S. Jang, L. Tran, J. S. Lee, H. Bae, S. W. Shin and M. P. Suryawanshi, *ACS Appl. Mater. Interfaces*, 2023, **5,** 21123–21133.
3. T. Shen, J. Tian, L. Lv, C. Fei, Y. Wang, T. Pullerits and G. Cao, *Electrochim. Acta*, 2016, **191,** 62–69.
4. J. Huang, G. Hu, Y. Ding, M. Pang and B. Ma, *J. Catal.*, 2016, **340,** 261–269.
5. P. Anushkkaran, T. S. Koh, W. S. Chae, H. H. Lee, S. H. Choi and J. S. Jang, *ACS Sustain. Chem. Eng.*, 2023, **11,** 5895–5907.
6. L. Mao, H. Deng, M. Li and S. Shen, *Sci. China Mater.*, 2023, **66,** 603–613.
7. J. Xiao, C. Li, X. Jia, B. Du, R. Li and B. Wang, *J. Colloid Interface Sci.*, 2022, **633,** 555–565.
8. B. Lei, D. Xu, B. Wei, T. Xie, C. Xiao, W. Ji and L. Xu, *ACS Appl. Mater. Interfaces*, 2021, **13,** 4785–4795.
9. I. S. Hwang, M. A. Mahadik, M. S. Song, S. W. Lee, B. T. Oh, H. H. Lee, W. S. Chae, S. H. Choi and J. S. Jang, J. *Environ. Chem. Eng.*, 2023, **11,** 109985.
10. R. Chong, Z. Wang, J. Lv, J. Rong, L. Zhang, Y. Jia, L. Wang, Z. Chang and X. Wang, *J. Catal.*, 2021, **399,** 170–181.